

Diffusio-osmotic corner flows

Dobromir Nowak^{1,2} and Maciej Lisicki¹

¹Faculty of Physics, University of Warsaw, Pasteura 5, Warsaw 02-093, Poland

²Department of Applied Physics, University of Geneva, Rue de l'Ecole-De-Médecine 20, Geneva 1205, Switzerland

Corresponding author: Maciej Lisicki, mklis@fuw.edu.pl

(Received 26 August 2025; revised 7 December 2025; accepted 15 December 2025)

We study flows generated within a two-dimensional corner by the chemical activity of the confining boundaries. Catalytic reactions at the surfaces induce diffusio-osmotic motion of the viscous fluid throughout the domain. The presence of chemically active sectors can give rise to steady eddies reminiscent of classical Moffatt vortices, which are mechanically induced in similar confined geometries. In our approach, an exact analytical solution of the diffusion problem in a wedge geometry is derived and coupled to the diffusio-osmotic slip-velocity formulation, yielding the stream function of associated Stokes flow. In selected limiting cases, simple closed-form expressions provide clear physical insight into the underlying mechanisms. Our results open new perspectives for the design of microscale mixing strategies in dead-end pores and cornered microfluidic channels, and offer benchmarks for numerical simulations of confined (diffusio-)osmotic systems.

Key words: low-Reynolds-number flows, coupled diffusion and flow, microfluidics

1. Introduction

The microscale manipulation of flowing fluids remains at the core of multiple modern applications, from microfluidic appliances in diagnostics and substance testing, to small-scale chemical synthesis and industrial precision manufacturing technologies. In Stokes flow conditions appropriate for sub-millimetre fluidic systems, flow can be controlled globally by imposing external forces or pressure gradients that induce laminar flow with only little mixing due to molecular diffusion. While easy to control, global forcing mechanisms pose challenges for applications that require local mixing, selective pumping, or the manipulation of suspended particles within confined environments (Squires & Quake 2005). On the other hand, biological and nanorobotic actuation mechanisms, such

as ciliated surfaces, rely on localised forcing to achieve swimming, pumping, mixing, nutrient capture, and sensing (Gilpin, Bull & Prakash 2020; Omori & Ishikawa 2025). In these settings, surface forcing becomes the key driver of macroscopic bulk flow. In confined geometry, such as in microchannels or pores, this mechanical activity is often coupled to the geometry of the flow domain, and the resulting asymmetry is responsible for creating flow.

A promising approach exploits phoretic mechanisms, in which surface-generated gradients (of concentration, temperature, etc.) induce effective slip flow on confining surfaces, which in turn gives rise to bulk flow (Anderson 1989). Diffusio-osmosis and diffusio-phoresis, the motion of particles and fluids in response to solute concentration gradients (Golestanian, Liverpool & Ajdari 2007; Jülicher & Prost 2009; Sabass & Seifert 2012), is now a well-established active propulsion mechanism, with numerous applications in artificial active matter (Bechinger *et al.* 2016; Shim 2022).

The presence of local chemical gradients in microfluidic channels can lead to cooperation or competition with global advective flow, enabling size-dependent colloid transport (Shin *et al.* 2016), or particle focusing that can be precisely tuned through the interplay of channel geometry, confinement, and surface chemical activity (Ault, Shin & Stone 2018). Diffusio-phoresis has also been used to organise colloids into sharp bands (Staffeld & Quinn 1989), to boost the migration of large particles via imposed solute contrasts (Abécassis *et al.* 2008), and to rectify particle motion to yield motility and pattern formation (Palacci *et al.* 2010). Subsequent microfluidic studies revealed steady-state focusing in multicomponent gradients (Shi *et al.* 2016). In colloids–salt mixtures, phoretic effects were shown to affect mixing (Raynal & Volk 2019), potentially leading to flow effects ranging from enhanced dispersion to blockage in cellular flows (Volk *et al.* 2022). The coupling of hydrodynamic flows and phoresis can further tune chemotactic and diffusio-phoretic spreading (Chu *et al.* 2022).

In microscale channels, the presence of dead-end pores can be used to induce a concentration difference between the main channel and pores large enough to entrain particles (Wilson *et al.* 2020), or capture and retain them (Battat *et al.* 2019; Akdeniz, Wood & Lammertink 2023), affecting filtration and dispersion in porous media (Alessio *et al.* 2021; Chu *et al.* 2021; Doan *et al.* 2021; Sambamoorthy & Chu 2023; Somasundar *et al.* 2023; Teng, Rallabandi & Ault 2023; Alipour *et al.* 2024; Jotkar *et al.* 2024; Sambamoorthy & Chu 2025). Such diffusio-phoretic mechanisms have been shown to enhance solute and particle transport into and out of dead-end pores (Kar *et al.* 2015), and to enable size-dependent control of colloidal trapping and release via solute gradients in confined geometries (Shin *et al.* 2016), with recent simulations and analyses further quantifying phoretic transport and mixing in narrow channels (Bhattacharyya, Sengupta & Chakraborty 2023; Migacz, Castleberry & Ault 2024; Visan, Wood & Lammertink 2024). Active or catalytic pores have also been proposed as local pumps and mixers capable of driving sustained fluid transport without external pressure gradients (Antunes *et al.* 2022, 2023; Bhattacharyya *et al.* 2023; Migacz *et al.* 2024; Tiwari *et al.* 2025). When considering catalytic active surfaces, geometric asymmetry alone is sufficient to create heterogeneous concentration fields that can induce propulsion (Michelin & Lauga 2015; Lisicki, Reigh & Lauga 2018) or pumping (Michelin *et al.* 2015; Lisicki, Michelin & Lauga 2016; Michelin & Lauga 2019; Yu *et al.* 2020). Since recent advances in fabrication allow for precise spatial patterning of active regions on surfaces, e.g. with catalysts (Archer, Campbell & Ebbens 2015; Kreienbrink *et al.* 2025), enzymes (Sengupta *et al.* 2014) or surface charges (Stroock *et al.* 2000; Stroock & Whitesides 2003), non-uniform coverage can be used together with geometric features to control microscale flow locally.

Here, we focus on a planar wedge-like geometry of dead-end pores, the walls of which are endowed with chemical activity, and which are filled with viscous fluid. Moffatt (1964a,b) was the first to examine the effect of this confinement on a flow that emerges in response to a disturbance that acts far away from the tip of the wedge, as well as from a mechanically active sector on the surface, imposing a slip flow on the boundary. In both cases, the celebrated Moffatt eddies emerge as a solution, with an infinite sequence of vortices being created in the fluid, as later seen experimentally by Taneda (1979). Self-similar vortical solutions emerge frequently in externally forced confined flows, such as wedge-shaped trenches with a free surface (Liu & Joseph 1977), cone-like geometry (Shankar 2005), electrohydrodynamic flows (He, Sun & Zhang 2022), simulations of driven cavity flows (Biswas & Kalita 2018; Polychronopoulos & Vlachopoulos 2018), and in ice flows over subglacial mountain valleys (Meyer & Creyts 2017). The classical problem of flow actuation by moving boundaries is perhaps best illustrated in the context of corner flows by Taylor's scraper problem (Taylor 1962), where one moving boundary 'scrapes' the fluid, causing its outward motion along the immobile wall. Moffatt's analysis of corner flow driven by a partial slip on the walls (Moffatt 1964b), akin to conveyor belts shearing the fluid locally, is an example of (local) mechanical actuation. Here, we explore a similar concept with a chemical actuation mechanism that couples to flow through diffusio-osmosis. We note that the problem of flow in the corner geometry can be treated as a limit of linear elasticity theory for a medium enclosed in wedge-like confinement. For the latter, the Green's functions have recently been found by Daddi-Moussa-Ider & Menzel (2025) and Daddi-Moussa-Ider *et al.* (2025). For low-Reynolds-number flows, asymptotic behaviour of the Stokeslet singularity in a corner were discussed extensively by Dauparas & Lauga (2018), and the method of images was used by Sprenger & Menzel (2023) to explore the dynamics of confined microswimmers.

In this work, we consider a non-uniform coverage of the wedge with a catalyst that induces the release or capture of solute. The heterogeneous concentration field, emerging from geometric asymmetry of the fluid domain, drives slip flow on the active surfaces, which in turn induces bulk flow that takes the form of a sequence of vortices. We calculate the flow analytically in the simplest cases. Next, using the Mellin transform formalism, we present an approach that applies to any coverage of the walls with chemical activity.

The paper is structured as follows. First, in § 2, we present the general mathematical framework of diffusio-osmotic Stokes flows, and describe the geometry of the problem and the relevant physical quantities. In § 3, we discuss the general solutions of the diffusion equation for the solute and the biharmonic equation for the flow stream function in the wedge geometry. We also introduce the formalism of Mellin transforms suited to the geometry considered. Next, in § 4, we present analytical solutions for the diffusio-osmotic flows induced by uniform coverage of one or both walls with a catalyst. In § 5, we discuss the solute concentration field emerging with a single active sector on one of the walls and the other boundary being absorbing, for different geometric settings. The complementary problem of diffusion with an active sector and a reflective boundary is treated in § 6. Finally, we show in § 7 how the solute concentration fields translate to the flow, and obtain the flow field numerically by solving for the stream function. Additionally, in § 8 we discuss the case of the chemical activity of the walls given by analytical functions rather than patches, represented by step-like profiles. We conclude the paper in § 9.

2. Generation of diffusio-osmotic flows

2.1. General framework

We adopt a continuum description of diffusio-osmotic transport, following established theoretical frameworks (Golestanian *et al.* 2007; Jülicher & Prost 2009; Sabass & Seifert 2012), to analyse the two-dimensional flow field generated within a wedge formed by two semi-infinite lines starting from one point. The fluid within the wedge is characterised by dynamic viscosity η and density ρ_0 , and contains solute of local concentration \tilde{C} (number of particles per unit volume), with diffusivity κ . The chemical activity \mathcal{A} of a surface \mathcal{S} quantifies the fixed rate of solute release ($\mathcal{A} > 0$) or absorption ($\mathcal{A} < 0$) on the surface by

$$\kappa \mathbf{n} \cdot \nabla \tilde{C} = -\mathcal{A} \quad \text{on } \mathcal{S}, \quad (2.1)$$

where \mathbf{n} is the normal unit vector on \mathcal{S} . Due to the short-range interaction of solute molecules with the cavity boundary, local concentration gradients result in the motion of the solute, and consequently drive the motion of the fluid (Anderson 1989). Assuming that the thickness of the interaction layer is small compared to the dimensions of the cavity, the classical slip-velocity formulation can be used (Michelin & Lauga 2014), and local solute gradients induce an effective slip velocity on the boundaries,

$$\tilde{\mathbf{u}} = \mathcal{M}(\mathbf{1} - \mathbf{n}\mathbf{n}) \cdot \nabla \tilde{C} \quad \text{on } \mathcal{S}, \quad (2.2)$$

which drives the bulk motion of the fluid. Here, \mathcal{M} is the local phoretic mobility at the surface \mathcal{S} . It is related to the surface–solute interaction potential (Anderson 1989).

Introducing \mathcal{R} as the characteristic length scale, and $\mathcal{U} = |\mathcal{A}\mathcal{M}|/\kappa$ as the characteristic phoretic velocity generated along \mathcal{S} , we can define the Péclet and Reynolds numbers

$$Pe = \frac{\mathcal{U}\mathcal{R}}{\kappa}, \quad Re = \frac{\rho_0 \mathcal{U}\mathcal{R}}{\eta}, \quad (2.3)$$

which quantify, respectively, the relative importance of solute advection and diffusion as transport mechanisms and effects of inertia and viscosity in forces that shape the flow. When Pe is small enough, the solute dynamics is purely diffusive and is governed by Laplace's equation

$$\nabla^2 \tilde{C} = 0, \quad (2.4)$$

in the whole domain. Provided that inertial effects are negligible (i.e. $Re \ll 1$), the flow and pressure fields satisfy the incompressible Stokes equations:

$$\eta \nabla^2 \tilde{\mathbf{u}} = \nabla \tilde{P}, \quad (2.5)$$

$$\nabla \cdot \tilde{\mathbf{u}} = 0. \quad (2.6)$$

The diffusive Laplace's problem for the solute concentration \tilde{C} effectively decouples from the hydrodynamic problem and may be solved independently. The concentration \tilde{C} can be used to compute the slip flow along \mathcal{S} via (2.2), which serves as the boundary condition for the flow field in (2.5) within the cavity.

We note here that while the fluid is assumed incompressible, in phoretic problems involving the transport of particles, effective particle velocity fields can appear compressible due to concentration-dependent drift. For instance, Raynal *et al.* (2018) showed that diffusio-phoretic drift can induce an effectively compressible colloid flow, even in an incompressible solvent, leading to transient particle focusing. Similarly, Chu *et al.* (2020) studied colloid transport under transient solute gradients where spatially

varying drift produces apparent compression or expansion, though the underlying fluid remains incompressible.

Given the boundary conditions that we assume in this problem, and the governing Laplace equation, if \tilde{C}_0 is a constant and the concentration field \tilde{C} is a solution, then the excess concentration $\tilde{c} = \tilde{C} - \tilde{C}_0$ is a solution too. The boundary conditions (2.1) and (2.2) do not depend on the absolute value of the local concentration. For all \tilde{C}_0 , the resulting flow will be the same. This also implies that \tilde{c} can be negative. After shifting by a positive \tilde{C}_0 , we thus will still obtain a physical solution. In the following subsections, we will therefore replace concentration \tilde{C} with field \tilde{c} .

2.2. Non-dimensionalisation of the model

We have already defined \mathcal{U} and \mathcal{R} as the characteristic velocity and length. The choice of the characteristic length depends on the problem at hand – we discuss this in detail when defining specific problems, but in general it may be set e.g. by the size of an active patch on the wall. Since \tilde{c} is the excess concentration, its variations scale with the magnitude of the gradients produced at confining boundaries, which are induced by surface chemistry. Its natural scale is therefore $\mathcal{C} = |\mathcal{A}| \mathcal{R}/\kappa$, where $|\mathcal{A}|$ is the typical magnitude of the chemical surface activity. The characteristic pressure is constructed from the typical velocity scale, given by the mobility and the magnitude of concentration, and reads $\mathcal{P} = \eta |\mathcal{A} \mathcal{M}|/\mathcal{R} \kappa$. The dimensionless pressure, concentration and velocity fields are thus given by $P = \tilde{P}/\mathcal{P}$, $c = \tilde{c}/\mathcal{C}$ and $\mathbf{u} = \tilde{\mathbf{u}}/\mathcal{U}$. Similarly, the dimensionless activity and mobility are given by $A = \mathcal{A}/|\mathcal{A}|$ and $M = \mathcal{M}/|\mathcal{M}|$. Since activity can vary over the surface \mathcal{S} , the choice of the characteristic activity is not always obvious. Because $Pe, Re \propto |\mathcal{A}|$, choosing the maximal value of $|\mathcal{A}|$ on the surface \mathcal{S} leads to the strongest conditions on Pe and Re . For the diffusion of solute, the non-dimensional governing equations are

$$\nabla^2 c = 0, \quad (2.7a)$$

$$\mathbf{n} \cdot \nabla c = -A \quad \text{on} \quad \mathcal{S}, \quad (2.7b)$$

while the flow problem becomes

$$\nabla^2 \mathbf{u} = \nabla P, \quad (2.7c)$$

$$\nabla \cdot \mathbf{u} = 0, \quad (2.7d)$$

$$\mathbf{u} = M(\mathbf{1} - \mathbf{n}\mathbf{n}) \cdot \nabla c \quad \text{on} \quad \mathcal{S}. \quad (2.7e)$$

In the following, we apply this general framework to the specific geometry of a narrowing corner to explore the ways in which fluid motion can be actuated within such a cavity by purely chemical means, with no moving mechanical parts.

3. Corner flows

The problem of osmotic flow generation in a wedge qualitatively resembles that leading to Moffatt eddies (Moffatt 1964a,b). In the classical problem analysed by Moffatt (1964a), an infinite sequence of eddies is formed in a wedge-shaped planar domain filled with viscous fluid due to a disturbance acting at asymptotically large distances from the corner. Eddies emerge as a self-similar solution to a second-kind eigenvalue problem for the stream function. However, similar flow structures can arise when the fluid is actuated by a moving boundary, as in the famous Taylor's scraper problem (Taylor 1962), where one of the walls of the wedge-shaped cavity moves with constant speed and drives macroscopic flow. A refined variant of this geometric setting involves motion of a portion of the boundary, when a section of it is endowed with slip velocity, as explored by Moffatt (1964b). Using Mellin

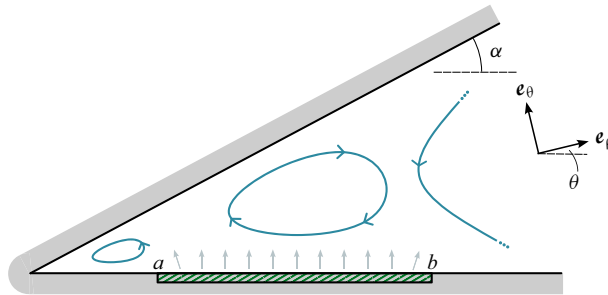


Figure 1. Geometry of the diffusio-osmotic corner flow set-up in polar coordinates (ρ, θ) . In a wedge of opening angle α , an active patch on the $\theta = 0$ wall covering the radial section $\rho \in [a, b]$ releases solute (grey arrows) and generates an inhomogeneous concentration field that drives circulatory flow indicated by schematic streamlines.

transform techniques, Moffatt found a solution of this problem for a single moving region (and two regions placed symmetrically), corresponding to transmission belts mounted within the walls. The solution again involves a sequence of corner eddies. This mechanical example operates using the same principle as one implemented in our case.

Here, we focus on a similar geometry but allow the walls to exhibit chemical activity, which drives the flow. The diffusio-osmotic flow generation mechanism leads, in general, to a non-uniform slip velocity profile on the bounding walls. However, for the case of uniform coverage of either one or both walls with catalyst, the induced slip velocity remains constant, therefore directly reducing to the previously obtained results. As we demonstrate analytically in the following, both antisymmetric and symmetric flows can be induced, depending on the specific coverage pattern.

3.1. Solute concentration

We first focus on the problem of diffusion of a solute in the corner domain. Upon introducing cylindrical polar coordinates (ρ, θ) (see figure 1), the stationary Laplace's equation for the concentration field c takes the form

$$\rho \frac{\partial}{\partial \rho} \left(\rho \frac{\partial c}{\partial \rho} \right) + \frac{\partial^2 c}{\partial \theta^2} = 0. \quad (3.1)$$

Suppose that the wedge extends in polar coordinates from $\theta = 0$ to $\theta = \alpha$. The boundary conditions are imposed on the normal gradient of concentration, $\mathbf{n} \cdot \nabla c$, and are thus given by the chemical activity distribution on the walls, $A_0(\rho)$ and $A_\alpha(\rho)$, as

$$\frac{1}{\rho} \frac{\partial c}{\partial \theta} = -A_0(\rho), \quad (3.2)$$

if the condition is imposed on the wall $\theta = 0$, and

$$\frac{1}{\rho} \frac{\partial c}{\partial \theta} = A_\alpha(\rho), \quad (3.3)$$

if the condition is imposed on the wall $\theta = \alpha$. For the two-dimensional diffusion equation to be well-posed, we require the integrals of both activity functions over the walls to add to zero, as we discuss later in the paper.

3.2. Stokes flow

Once the concentration distribution $c(\rho, \theta)$ is known, the slip flow velocity $\mathbf{u}_s = u_s \mathbf{e}_\rho$ on the boundary is determined as

$$u_s = M \frac{\partial c}{\partial \rho} \Big|_S, \quad (3.4)$$

which becomes the boundary condition for a two-dimensional flow in the fluid domain. In this problem, it is convenient to introduce the two-dimensional stream function $\Psi(\rho, \theta)$ (Batchelor 2000; Deville 2022) such that in polar coordinates,

$$u_\rho = \frac{1}{\rho} \frac{\partial \Psi}{\partial \theta}, \quad u_\theta = -\frac{\partial \Psi}{\partial \rho}. \quad (3.5)$$

Since $\mathbf{u} = (u_\rho, u_\theta)$ satisfies the incompressible Stokes equations (2.7c)–(2.7d), Ψ obeys the biharmonic equation

$$\nabla^4 \Psi = 0, \quad (3.6)$$

with the boundary conditions on the two planes $\theta = \{0, \alpha\}$ being

$$u_\rho = \frac{1}{\rho} \frac{\partial \Psi}{\partial \theta} = u_s, \quad u_\theta = -\frac{\partial \Psi}{\partial \rho} = 0, \quad \text{for } \theta = \{0, \alpha\}. \quad (3.7)$$

3.3. Solution of Laplace and biharmonic equations in the Mellin space

We now introduce the formalism of Mellin transforms (Butzer & Jansche 1997; Debnath & Bhatta 2016) to solve the more general case of a single active sector. Indeed, Mellin transforms have become the traditional method for solving boundary-value problems in wedge-shaped regions (Tranter 1948; Moffatt 1964a,b; Martin 2017). In cylindrical coordinates, Laplace's equation takes the form (3.1). We denote by $\bar{c}(p, \theta)$ the Mellin transform \mathcal{M}_p of concentration $c(\rho, \theta)$, where p is the transform variable, and

$$\mathcal{M}_p\{c(\rho, \theta)\} := \int_0^\infty \rho^{p-1} c(\rho, \theta) d\rho =: \bar{c}(p, \theta). \quad (3.8)$$

In addition, \mathcal{M}^{-1} is the inverse Mellin transform, which reads

$$c(\rho, \theta) = \mathcal{M}^{-1}\{\bar{c}(p, \theta)\} = \frac{1}{2\pi i} \int_{\gamma-i\infty}^{\gamma+i\infty} \bar{c}(p, \theta) \rho^{-p} dp. \quad (3.9)$$

The conditions for the existence of the inverse transform are that for a chosen parameter γ , the integral $\int_0^\infty \rho^{\gamma-1} c(\rho, \theta) d\rho$ exists, and the complex integration line $(\gamma - i\infty, \gamma + i\infty)$ lies within the strip of analyticity of $\bar{c}(p, \theta)$. When these conditions are satisfied, the inverse is independent of γ . Unless stated otherwise, we take $\gamma = 0$. Then, for appropriate $c(\rho, \theta)$, we have

$$\mathcal{M}_p\{\rho \partial_\rho c(\rho, \theta)\} = \mathcal{M}_{p+1}\{\partial_\rho c(\rho, \theta)\} = -p\bar{c}(p, \theta), \quad (3.10)$$

where we introduced an abbreviation for derivatives, $\partial_\rho \equiv \partial/\partial\rho$, etc. The Laplace equation for concentration, (3.1), implies that $p^2 \bar{c} + \partial_\theta^2 \bar{c} = 0$, and for some $C(p)$, $D(p)$, we have

$$\bar{c}(p, \theta) = C(p) e^{ip\theta} + D(p) e^{-ip\theta}. \quad (3.11)$$

We now turn to the flow problem. Let Ψ be the stream function. The biharmonic equation $\nabla^4 \Psi = 0$ in cylindrical coordinates and after applying the Mellin transform

\mathcal{M}_{p+4} becomes

$$\left\{ \partial_\theta^4 + [(p+2)^2 + p^2] \partial_\theta^2 + p^2(p+2)^2 \right\} \bar{\Psi}(p, \theta) = 0, \quad (3.12)$$

where we write $\bar{\Psi}(p, \theta) := \mathcal{M}_p\{\Psi(\rho, \theta)\}$. The general solution then reads

$$\bar{\Psi} = F_1(p) \cos(p\theta) + F_2(p) \sin(p\theta) + G_1(p) \cos((p+2)\theta) + G_2(p) \sin((p+2)\theta). \quad (3.13)$$

4. Phoretic walls with uniform coverage

To study the effect of chemical activity on corner flows, we first focus on the case when the coverage by catalyst is uniform, and the heterogeneity of the concentration field stems purely from the geometry of the wedge. In the two examples studied in the following, either one or both walls are active, and the problem admits analytical solutions. In this case, the problem has no natural length scale, and the velocity scale is given purely by the activity and mobility at the surface.

4.1. A single active wall

In the first simple example, we consider a single active wall, with constant activity A on the surface. To ensure the existence of a steady-state solution, we assume that the other boundary is absorbing, thus we can write the boundary conditions for the concentration problem as

$$\frac{\partial c}{\partial \theta} = -A\rho \quad \text{for } \theta = 0, \quad (4.1)$$

$$c = 0 \quad \text{for } \theta = \alpha. \quad (4.2)$$

Using the separated form $c = R(\rho) \Theta(\theta)$ as an ansatz, we find the general solution

$$R(\rho) = r_1 \rho^\lambda + r_2 \rho^{-\lambda}, \quad \Theta(\theta) = q_1 \cos \lambda \theta + q_2 \sin \lambda \theta, \quad (4.3)$$

where $r_1, r_2, q_1, q_2, \lambda$ are constants that need to be determined. Applying the boundary conditions, we obtain the concentration field as

$$c(\rho, \theta) = -\frac{A\rho \sin(\theta - \alpha)}{\cos \alpha}. \quad (4.4)$$

The fact that the concentration increases linearly with the distance from the tip is a consequence of the fixed flux boundary condition and the fact that the active patch extends to infinity. In reality, the finite size of the active patch limits the concentration field, as we discuss later. As a result, the tangential gradient of the concentration profile yields a constant slip velocity distribution on the surface,

$$\mathbf{u} = MA \tan \alpha \mathbf{e}_\rho \quad \text{for } \theta = 0, \quad (4.5)$$

$$\mathbf{u} = \mathbf{0} \quad \text{for } \theta = \alpha. \quad (4.6)$$

With this velocity profile, the problem becomes identical to the well-known Taylor's scraper (Taylor 1962), with the imposed slip velocity $U = MA \tan \alpha$. The stream function then has the form

$$\Psi = U\rho F(\theta), \quad (4.7)$$

where $F(\theta)$ satisfies an ordinary differential equation

$$F'''' + 2F'' + F = 0, \quad (4.8)$$

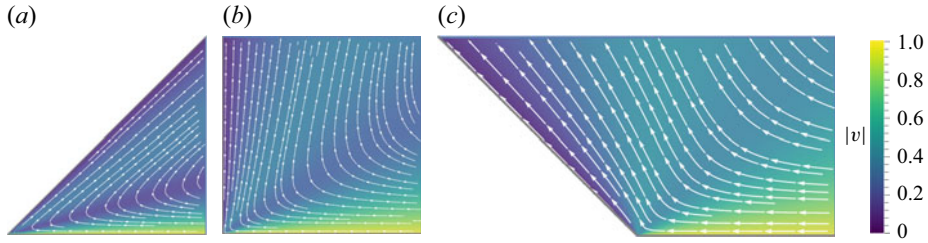


Figure 2. Diffusio-osmotic flow induced by the activity of one phoretic wall in a wedge of angle α for (a–c) $\alpha = \{\pi/4, \pi/2, 3\pi/4\}$, respectively. Flow streamlines are marked in white. The colour map indicates the total velocity magnitude. The emergent bulk flow remains comparable in magnitude to the driving slip flow on the active boundary, and decays rapidly close to the inert, no-slip wall.

with the boundary conditions $F(0) = 0$, $F'(0) = 1$, $F(\alpha) = 0$, $F'(\alpha) = 0$. We note that by (3.7), the boundary conditions for F correspond to the normal velocity at the surface, while those for F' pertain to the induced slip (tangential) velocity component. This is a particular form of the general solution to planar elasticity problems for the biharmonic Airy stress function due to Michell (1899). The resulting stream function reads

$$\Psi = U\rho F(\theta) = \frac{U\rho}{\alpha^2 - \sin^2 \alpha} [\alpha(\alpha - \theta) \sin \theta - \theta \sin \alpha \sin(\alpha - \theta)]. \quad (4.9)$$

The resulting flow fields are drawn in figure 2 for three values of the wedge opening angle $\alpha = \{\pi/4, \pi/2, 3\pi/4\}$. The flow is asymmetric, reflecting the boundary conditions. We observe the strongest flow along the active boundary, and a gradual decay of the velocity field closer to the other, no-slip wall. We note that the magnitude of the bulk velocity field remains a large fraction of the surface slip velocity, confirming the pronounced effect of surface actuation.

4.2. Two phoretic walls

A simple generalisation of the problem of one wall involves covering both walls of the wedge with catalyst, thereby imposing a slip velocity symmetrically for both $\theta = 0$ and $\theta = \alpha$. In this case, we expect the flow to be symmetrical about the wedge bisector.

The concentration profile satisfying the fixed-flux boundary conditions at both walls, namely,

$$\frac{\partial c}{\partial \theta} = -A\rho \quad \text{for } \theta = 0, \quad (4.10a)$$

$$\frac{\partial c}{\partial \theta} = A\rho \quad \text{for } \theta = \alpha, \quad (4.10b)$$

follows directly as

$$c(\rho, \theta) = A\rho \frac{\sin(\theta - \alpha) - \sin \theta}{1 - \cos \alpha}. \quad (4.11)$$

Equation (4.8) remains valid with the new boundary conditions $F(0) = F(\alpha) = 0$ (no normal velocity at the surface) and $F'(0) = F'(\alpha) = 1$ (two active walls with non-zero slip velocity). The stream function in this case takes on the form

$$\Psi = \frac{U\rho}{\alpha - \sin \alpha} [(\alpha - \theta) \sin \theta - \theta \sin(\alpha - \theta)]. \quad (4.12)$$

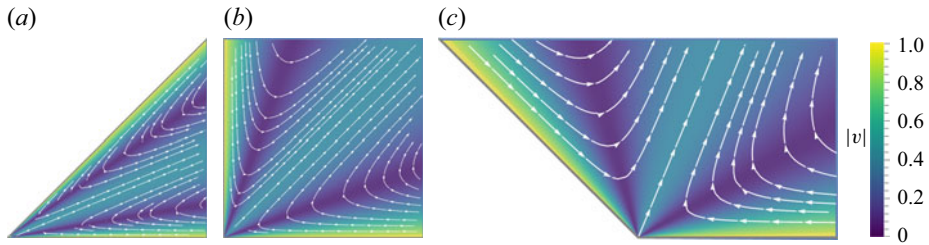


Figure 3. Diffusio-osmotic flow induced by the activity of two phoretic walls in a wedge of angle $\alpha = \{\pi/4, \pi/2, 3\pi/4\}$. The colour map indicates the total velocity magnitude. We note a strong flow close to the driving active boundaries, and a counterflow along the wedge bisector.

The resulting flow fields are drawn in figure 3 for three values of the wedge opening angle $\alpha = \{\pi/4, \pi/2, 3\pi/4\}$. The flow is symmetrical, with the fluid dragged along the walls towards the wedge vertex, and expelled along the bisector.

5. The diffusion problem with an active and absorbing wall

To explore the flow in a more general case, we focus on a corner with a single active sector of length $\ell = b - a$ placed on one of the boundaries at a distance a (between $\rho = a$ and $\rho = b$), as depicted in figure 1. The other wall is perfectly absorbing. Contrary to the previous cases, the problem now has two natural length scales: ℓ and a .

The concentration field satisfies the Laplace equation $\nabla^2 c = 0$ with the boundary conditions

$$\frac{\partial c}{\partial \theta} = -A\rho \mathbb{1}_{[a,b]} \quad \text{for } \theta = 0, \quad (5.1a)$$

$$c = 0 \quad \text{for } \theta = \alpha, \quad (5.1b)$$

where $\mathbb{1}_{[a,b]}$ is the indicator function of set $[a, b]$.

5.1. The case $a \neq 0$ and $b < \infty$

The solution in Mellin space is

$$\bar{c}(p, \theta) = A \frac{b^{p+1} - a^{p+1}}{p(p+1)} \frac{\sin(p(\alpha - \theta))}{\cos p\alpha}. \quad (5.2)$$

It is assumed that $0 < \alpha < 2\pi$. The solution has singularities at p'_k such that $p'_k \alpha = \pi/2 + k\pi$ for $k \in \mathbb{Z}$, and also at $p_0 = -1$, and a removable singularity at $p = 0$.

To evaluate the concentration field, we must now invert the Mellin transform. The concentration in the real space can be written as $c = I_b - I_a$, where

$$f_a = A \frac{a}{p(p+1)} \frac{\sin(p(\alpha - \theta))}{\cos p\alpha} \left(\frac{a}{\rho}\right)^p, \quad (5.3)$$

$$I_a = \frac{1}{2\pi i} \int_{\gamma-i\infty}^{\gamma+i\infty} f_a dp. \quad (5.4)$$

The complex integral above can be evaluated by applying Cauchy's residue theorem to a square integration contour sketched in figure 4. For $a \leq \rho$, the integration contour lies in the half-plane $Re(p) > \gamma$. For $a > \rho$, the appropriate contour lies in the $Re(p) < \gamma$ half-plane. Such a choice ensures that the integral over three sides of the square contour vanishes when the contour is extended to infinity.

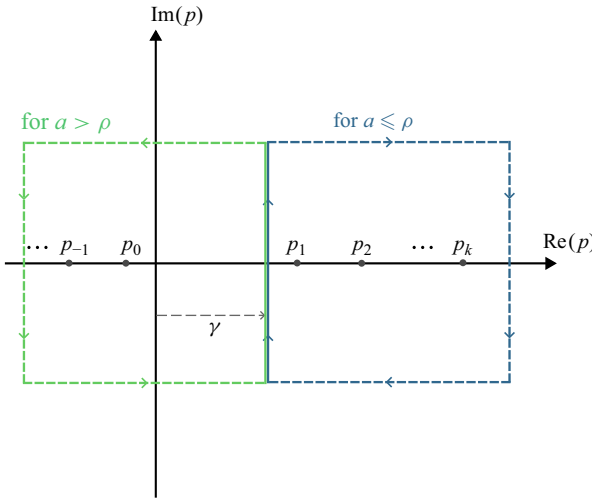


Figure 4. Contours of integration for the evaluation of the inverse Mellin transform. The green contour is used for $a > \rho$, and the blue contour for $a \leq \rho$. Both integration contours are shifted by γ along the real axis, and the poles of the integrand are denoted by p_k , where $k \in \mathbb{Z}$. To evaluate the integral, one takes the limit of the square side length approaching infinity. In the limit, contributions from the three dashed sides of each square contour vanish, and the desired integral along the imaginary axis can be evaluated using the method of residues.

In particular, for the integral in (5.4), we select $\gamma = 0$. The poles are listed as

$$p_k = \begin{cases} \alpha^{-1} \left(\frac{\pi}{2} + (k-1)\pi \right) & \text{for } k \in \mathbb{Z}_+, \\ -1 & \text{for } k = 0, \\ \alpha^{-1} \left(-\frac{\pi}{2} + (k+1)\pi \right) & \text{for } k \in \mathbb{Z}_-. \end{cases} \quad (5.5)$$

Under the assumption that for all k , $((\pi/2) + k\pi)/\alpha \neq -1$ (i.e. $\alpha \neq \pi/2, \pi, 3\pi/2$), the residues are

$$\text{for } k \neq 0, \quad \text{Res}_{p=p_k} f_a = -\frac{Aa}{\alpha p_k(p_k+1)} \cos(p_k \theta) \left(\frac{a}{\rho}\right)^{p_k}, \quad (5.6a)$$

$$\text{for } k = 0, \quad \text{Res}_{p=p_k} f_a = A \frac{\sin(\alpha - \theta)}{\cos \alpha} \rho. \quad (5.6b)$$

Depending on the ratio a/ρ , different residues are contained in the integration contour, and the orientation of the contour is different, hence

$$I_a(\rho, \theta) = \begin{cases} \sum_{k \leq 0} \text{Res}_{p=p_k} f_a & \text{for } a > \rho, \\ -\sum_{k \geq 1} \text{Res}_{p=p_k} f_a & \text{otherwise,} \end{cases} \quad (5.7)$$

with the full solution being

$$c(\rho, \theta) = I_b(\rho, \theta) - I_a(\rho, \theta). \quad (5.8)$$

Note that the residue at $p = -1$ is responsible for satisfying the condition (5.1a). In the special cases $\alpha = \pi/2, \pi, 3\pi/2$, solutions can be obtained by taking, for example, the limit of $\alpha \rightarrow \pi/2$. The solutions for $\alpha = \pi/2 - \epsilon$ and $\alpha = \pi/2 + \epsilon$ can then be compared to check if the desired accuracy has been achieved for a chosen small parameter ϵ .

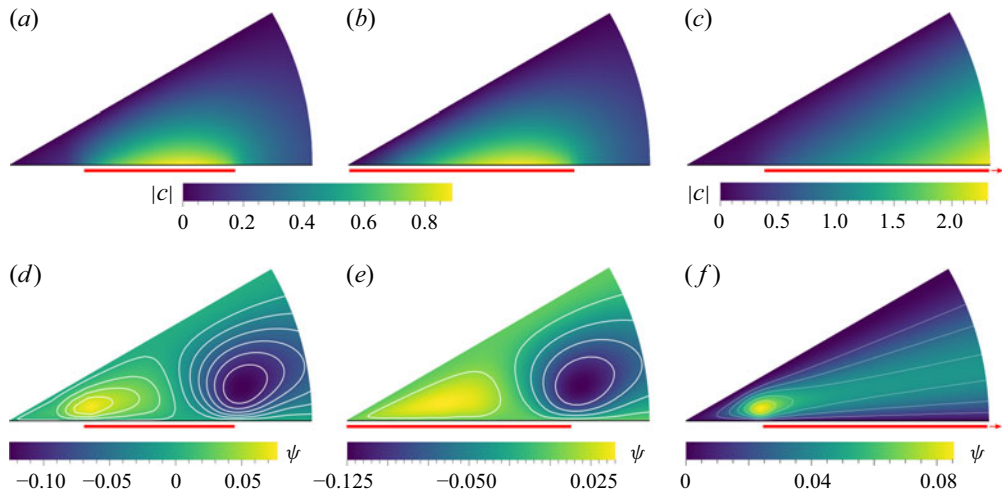


Figure 5. (a–c) Solute concentration fields, and (d–f) isolines of the stream function ψ , for an ideally absorptive wall at $\theta = \pi/6$ and a catalytic (active) wall at $\theta = 0$, with a catalytic sector at $(a, b) = \{(1, 3), (0, 3), (1, \infty)\}$ marked in red. Here, we assume $A = 1$, and the plotted radius of the wedge is $\rho < 4$. The scale bar for the absolute concentration field $|c|$ is common for plots (a,b) and different for (c).

5.2. The case $a = 0, b < \infty$, i.e. sector $[0, b]$

The solution is obtained similarly to the previous case as

$$c(\rho, \theta) = \begin{cases} \sum_{k \leq 0} \text{Res}_{p=p_k} f_b & \text{for } b > \rho, \\ -\sum_{k \geq 1} \text{Res}_{p=p_k} f_b & \text{otherwise.} \end{cases} \quad (5.9)$$

5.3. The case $a \neq 0$ and $b = \infty$, i.e. sector $[a, \infty]$

In this case, existence of the Mellin transform requires that $\gamma < -1$.

We thus take any γ such that $-1 > \gamma > -\pi/2\alpha$, and write the solution as

$$c(\rho, \theta) = \begin{cases} -\sum_{k \leq -1} \text{Res}_{p=p_k} f_a & \text{for } a > \rho, \\ \sum_{k \geq 0} \text{Res}_{p=p_k} f_a & \text{otherwise.} \end{cases} \quad (5.10)$$

A simple computation shows that in all the cases above, $c(\rho, \theta)$ with an appropriate choice of γ satisfies the condition for the existence of the inverse transform.

In figure 5, we sketch the solutions for the concentration field for a chosen wedge opening angle $\theta = \pi/6$ in three representative cases. The catalytic sector is marked in red, and the colours indicate the absolute value of solute concentration. In all cases, the resulting concentration field is heterogeneous, which offers the possibility to drive slip flow along the active boundary.

6. The diffusion problem with an active wall and a reflective wall

6.1. Solution for a single catalytic sector with reflective walls

Consider a setting in which the wall at $\theta = 0$ contains a catalytic sector with activity A and the wall at $\theta = \alpha$ is not active, thus it is a reflective wall, with no-flux boundary condition. We denote the corresponding solute concentration field by c_0 . The boundary conditions

are then

$$\frac{\partial c_0}{\partial \theta} = -A\rho \mathbb{1}_{[a,b]} \quad \text{for } \theta = 0, \quad (6.1a)$$

$$\frac{\partial c_0}{\partial \theta} = 0 \quad \text{for } \theta = \alpha. \quad (6.1b)$$

We again assume that $0 < \alpha < 2\pi$. A solution satisfying these boundary conditions in the Mellin space reads

$$\bar{c}_0(p, \theta) = -A \frac{b^{p+1} - a^{p+1}}{p(p+1)} \frac{\cos(p(\alpha - \theta))}{\sin(p\alpha)}. \quad (6.2)$$

If c_α is a solution for the active sector with activity A on the wall $\theta = \alpha$, i.e. for the boundary conditions

$$\frac{\partial c_\alpha}{\partial \theta} = 0 \quad \text{for } \theta = 0, \quad (6.3a)$$

$$\frac{\partial c_\alpha}{\partial \theta} = A\rho \mathbb{1}_{[a,b]} \quad \text{for } \theta = \alpha, \quad (6.3b)$$

then the corresponding solution takes the form

$$\bar{c}_\alpha(p, \theta) = \bar{c}_0(p, \alpha - \theta) = -A \frac{b^{p+1} - a^{p+1}}{p(p+1)} \frac{\cos(p\theta)}{\sin(p\alpha)}. \quad (6.4)$$

Let us introduce the notation

$$g_a(p, \theta) = -A \frac{a}{p(p+1)} \frac{\cos(p(\alpha - \theta))}{\sin(p\alpha)} \left(\frac{a}{\rho}\right)^p, \quad (6.5)$$

$$I_a = \frac{1}{2\pi i} \int_{\gamma-i\infty}^{\gamma+i\infty} g_a dp. \quad (6.6)$$

Applying the inverse Mellin transform to the solution (6.2), we can write

$$c_0 = I_b - I_a = \frac{1}{2\pi i} \int_{\gamma-i\infty}^{\gamma+i\infty} (g_b - g_a) dp. \quad (6.7)$$

We now note that g_a has poles at $p'_k = k\pi/\alpha$, with $k \in \mathbb{Z}$, and at $p = -1$. Under the assumption that for all k , $p'_k \neq -1$ (i.e. $\alpha \neq \pi$), the residues are

$$\text{for } k \neq 0, \quad \text{Res}_{p=p'_k} g_a = -\frac{Aa}{\alpha} \frac{\cos(p_k(\alpha - \theta))}{p_k(p_k + 1)} \left(\frac{a}{\rho}\right)^{p_k}, \quad (6.8a)$$

$$\text{for } k = 0, \quad \text{Res}_{p=0} g_a = -\frac{Aa}{\alpha} \left[\log\left(\frac{a}{\rho}\right) - 1 \right], \quad (6.8b)$$

$$\text{for } p = -1, \quad \text{Res}_{p=-1} g_a = -A\rho \frac{\cos(\alpha - \theta)}{\sin \alpha}. \quad (6.8c)$$

The choice of γ such that $\max\{p'_k : p'_k < 0\} = -\pi/\alpha < \gamma < 0$, $\gamma > -1$, guarantees that the Mellin transform of c_0 exists. Integrating over a square contour in one of the half-planes, we obtain

$$I_a(\rho, \theta) = \begin{cases} \sum_{k \leq -1} \text{Res}_{p=p'_k} g_a + \text{Res}_{p=-1} g_a & \text{for } a > \rho, \\ -\sum_{k \geq 0} \text{Res}_{p=p'_k} g_a & \text{otherwise.} \end{cases} \quad (6.9)$$

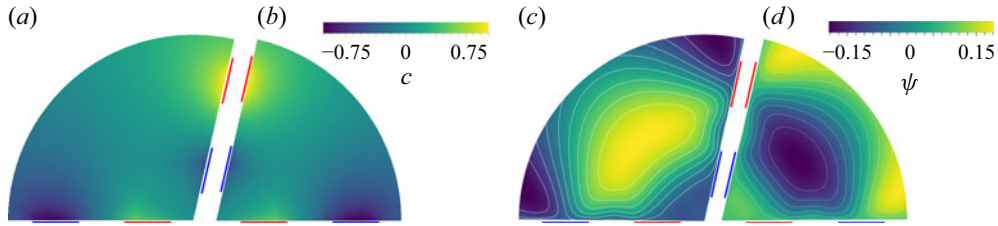


Figure 6. (a,b) Solute concentration fields, and (c,d) corresponding stream functions ψ , for wedges with multiple active sectors. The wedge angles are $\alpha = [4\pi/7, 3\pi/7]$. There are two active sectors of opposite activity $|A| = 1$ on each wall. They span the sections $\rho \in (0.5, 1.5)$ and $\rho \in (2.5, 3.5)$. The plotted radius of the wedge is $\rho < 4$. Patches of positive activity are marked in red, while those of negative activity are marked in blue. Panels (a,b) share the concentration scale bar placed in the middle of the figure, while the stream function scale bar for panels (c,d) is in the top right corner.

Using (6.7), c_0 can now be computed straightforwardly. The total activity of the walls not being zero does not cause a contradiction, since there are no constraints on activity at $\rho = \infty$, and the solute can be absorbed or emitted at infinity. The case $\alpha = \pi$ can be solved in Cartesian coordinates or by taking the limit $\alpha \rightarrow \pi$ in the above solution.

6.2. Diffusion for multiple catalytic sectors

By linearity, the solution can be obtained by superposition of solutions for single sectors. If sectors $[a_i, b_i]$ have activity A_i , then the condition for equilibrium is

$$\sum_i A_i (b_i - a_i) = 0, \quad (6.10)$$

where the sum is taken over all active sectors. This is also the condition for the solution to be physical (solute conservation), i.e. unless we allow the solute to be released/absorbed at $\rho = \infty$. It can be seen that the resulting solutions are indeed continuous. Note that the sectors can overlap, so step activity profiles can be created to mimic arbitrary activity functions $A_0(\rho)$ and $A_\alpha(\rho)$ of the walls.

An example of a setting involving multiple sectors is presented in figure 6 for two active patches of opposite activity on each of the walls, and for different wedge opening angles. The effect of activity of patches closer to the tip of the wedge is diminished by their mutual influence, and the concentration fields produced by patches further away from the confinement are more pronounced. This demonstrates the intricate interaction between the geometry of the wedge and the chemical activity of its walls.

6.3. The diffusion problem for an arbitrary catalytic wall

Let us now consider a setting where the wall at $\theta = 0$ has arbitrary activity $A = A(\rho)$, and the wall at $\theta = \alpha$ is reflective. We will approach this problem using the Green's function method (Arfken, Weber & Harris 2013), because the Stokes equation is linear. Let $c_0^G(\rho, \rho', \theta)$ be the Green's function, which is a formal solution to the Laplace equation with a point activity $\delta(\rho - \rho')$ at $\rho = \rho', \theta = 0$. Boundary conditions for $c_0^G(\rho, \rho', \theta)$ take the form

$$\frac{\partial c_0^G}{\partial \theta}(\rho, \rho', \theta) = -\rho \delta(\rho - \rho') \quad \text{for } \theta = 0, \quad (6.11a)$$

$$\frac{\partial c_0^G}{\partial \theta}(\rho, \rho', \theta) = 0 \quad \text{for } \theta = \alpha. \quad (6.11b)$$

The solution in the Mellin space reads

$$\bar{c}_0^G(p, \rho', \theta) = -\frac{\cos(p(\alpha - \theta))}{p \sin(p\alpha)} \rho'^p. \quad (6.12)$$

Here, $\bar{c}_0(p, \theta)$ is obtained by accounting for all point activities $A(\rho')\delta(\rho - \rho')$ along the boundary:

$$\bar{c}_0(p, \theta) = \int_0^\infty A(\rho') \bar{c}_0^G(p, \rho', \theta) d\rho'. \quad (6.13)$$

Residues of \bar{c}_0^G are $p_k = k\pi/\alpha$. We now change the order of integration in the back-transformed concentration field to arrive at

$$c_0(\rho, \theta) = \frac{1}{2\pi i} \int_0^\infty d\rho' A(\rho') \int_{\gamma-i\infty}^{\gamma+i\infty} -\frac{\cos(p(\alpha - \theta))}{p \sin(p\alpha)} \left(\frac{\rho'}{\rho}\right)^p dp, \quad (6.14)$$

where γ has to satisfy the same condition as in the previous section. Defining

$$h(p, \rho, \rho', \theta) = -\frac{\cos(p(\alpha - \theta))}{p \sin(p\alpha)} \left(\frac{\rho'}{\rho}\right)^p, \quad (6.15)$$

we evaluate the following residues:

$$\text{Res}_{p=p_k} h = \begin{cases} -\frac{1}{\alpha} \frac{\cos(p_k(\alpha - \theta))}{p_k} \left(\frac{\rho'}{\rho}\right)^{p_k} & \text{for } k \neq 0, \\ -\frac{1}{\alpha} \log\left(\frac{\rho'}{\rho}\right) & \text{for } k = 0. \end{cases} \quad (6.16)$$

Choosing the contours of integration the same way as in the previous section, we finally obtain

$$c_0(\rho, \theta) = \int_\rho^\infty d\rho' A(\rho') \sum_{k \leq -1} \text{Res}_{p_k} h(p, \rho, \rho', \theta) - \int_0^\rho d\rho' A(\rho') \sum_{k \geq 0} \text{Res}_{p_k} h(p, \rho, \rho', \theta). \quad (6.17)$$

We note that for two arbitrary catalytic walls, superposition of solutions can be used. The condition to satisfy solute conservation is

$$\int_0^\infty (A_0(\rho) + A_\alpha(\rho)) d\rho = 0, \quad (6.18)$$

where $A_0(\rho)$ and $A_\alpha(\rho)$ are the activities of the walls $\theta = 0$ and $\theta = \alpha$, respectively. It is worth noting that for practical purposes, approximating the solution for a given function $A(\rho)$ by making a superposition of solutions for constant activity sectors could potentially be more efficient than truncating the above series and evaluating the integrals.

7. Solution of the biharmonic equation for a given solute concentration field

Having resolved the concentration field in various cases and for different boundary conditions on each wall, we now turn to the calculation of the corresponding flow field. The boundary conditions for the stream function $\Psi(\rho, \theta)$, which satisfies the biharmonic equation (3.6), are

$$u_\theta = -\frac{\partial \Psi}{\partial \rho} = 0 \quad \text{for } \theta = 0, \alpha, \quad (7.1a)$$

$$u_\rho = \frac{1}{\rho} \frac{\partial \Psi}{\partial \theta} = M \frac{\partial c}{\partial \rho} \quad \text{for } \theta = 0, \alpha, \quad (7.1b)$$

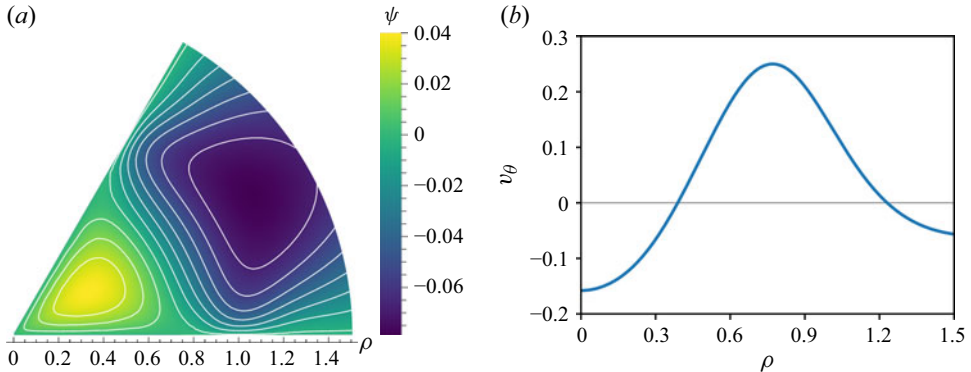


Figure 7. (a) Isolines of the stream function ψ of diffusio-osmotic corner flow for $\theta = \pi/3$, with active sectors at $\rho \in (0, 1)$, emitting at $\theta = 0$ and absorbing at $\theta = \alpha$. The flow in the corner eddy (yellow) is anticlockwise and drives clockwise rotation of another eddy further away from the corner. Colours code the magnitude of ψ . (b) Transversal velocity profile $v_\theta(\rho)$ on the bisector angle of the wedge. Roots of the velocity indicate the centres of vortices.

indicating that the only source of flow is the slip flow at the boundary, dictated by the heterogeneous solute concentration profile. Applying the Mellin transform \mathcal{M}_p to these conditions yields

$$\bar{\Psi} = 0 \quad \text{for } \theta = 0, \alpha, \quad (7.2a)$$

$$\frac{\partial \bar{\Psi}}{\partial \theta} = -pM\bar{c} \quad \text{for } \theta = 0, \alpha. \quad (7.2b)$$

Using the general form of the solution for $\bar{\Psi}$, given by (3.13), we may now identify the coefficients to be

$$G_1 = -F_1, \quad (7.3a)$$

$$\begin{bmatrix} F_1 \\ F_2 \\ G_2 \end{bmatrix} = \frac{-pM}{2D(p)} \bar{c}(p, 0) \begin{bmatrix} (p+1)\sin(2\alpha) - \sin(2\alpha(p+1)) \\ (p+1)\cos(2\alpha) + \cos(2\alpha(p+1)) - p - 2 \\ -p + (p+1)\cos(2\alpha) - \cos(2\alpha(p+1)) \end{bmatrix} + \frac{-pM}{2D(p)} \bar{c}(p, \alpha) \begin{bmatrix} (p+2)\sin(\alpha p) - p\sin(\alpha(p+2)) \\ -((p+2)(\cos(\alpha p) - \cos(\alpha(p+2)))) \\ p(\cos(\alpha p) - \cos(\alpha(p+2))) \end{bmatrix}, \quad (7.3b)$$

where $D(p) = (p+1)^2 \cos(2\alpha) - p(p+2) - \cos(2\alpha(p+1))$. The way to obtain $\bar{c}(p, 0)$ and $\bar{c}(p, \alpha)$ for an arbitrary setting of catalytic sectors on both walls has been demonstrated in previous sections. The remaining task is thus to invert the Mellin transform; this turns out to be challenging analytically, since zeros of $D(p)$ are difficult to obtain, unlike when inverting the Mellin transform for the concentration. We thus compute the integral (see (3.9)) numerically. In an illustrative case, where the active sectors on the walls span from the corner to $\rho = 1$, the calculated streamlines (the isolines of $\Psi(\rho, \theta)$) can be seen in figure 7. An anticlockwise eddy is created in the immediate vicinity of the active patches, and its rotation drives a larger eddy in the opposite direction further away from the corner. We note that this flow profile is obtained using only two active patches. When combined into more complicated coverage patterns, the flow can be tuned to a particular application, e.g. localised mixing.

It is useful to consider an experimentally practical scenario of the wedge opening angle $\alpha = \pi/2$, for which we present the flow field in figure 8. In this case, a single vortical

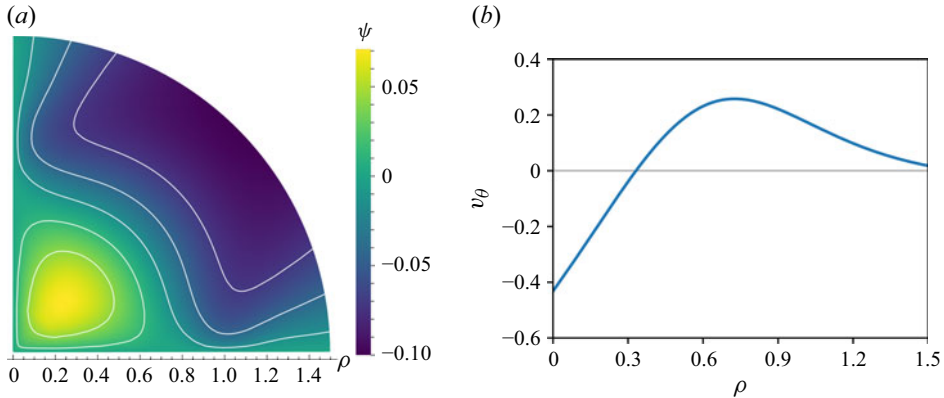


Figure 8. Diffusio-osmotic corner flow for the wedge opening angle $\pi/2$. (a) Isolines of the stream function show a single vortical structure in the corner. The active patches cover both walls close to the tip (for $\rho < 1$), with emission at the horizontal wall and absorption at the vertical surface. (b) Transversal velocity profile along the bisector line $\theta = \pi/4$.

structure emerges, fuelled by catalytic reactions on the walls close to the corner. The active patches cover the area $\rho < 1$ on both walls. The associated transversal velocity profile confirms that the vortex does not extend far beyond the active region.

8. Diffusion with analytic Neumann boundary conditions

Here, we present an auxiliary result for the diffusion problem when the activity patterns are given by analytic functions, rather than step-like profiles discussed earlier. Let $A^{(1)}(\rho)$ and $A^{(2)}(\rho)$ represent the (analytic) distribution of activity on the walls with $\theta = 0$ and $\theta = \alpha$, respectively. We make the following ansatz for the concentration profile c in the fluid domain,

$$c = \lambda_0 + \sum_{n \geq 1} (F_n \cos(n\theta) + G_n \sin(n\theta)) \rho^n, \quad (8.1)$$

and expand $A^{(1)}$ and $A^{(2)}$ in power series in ρ as

$$A^{(1)} = \sum_{n \geq 1} A_n^{(1)} \rho^n, \quad A^{(2)} = \sum_{n \geq 1} A_n^{(2)} \rho^n. \quad (8.2a)$$

Imposing the fixed flux boundary conditions (3.2) and (3.3), we arrive at linear equations for the coefficients of the expansion in (8.1). Solving these equations, we obtain

$$F_n = -\frac{A_{n-1}^{(1)} \cos(n\alpha) + A_{n-1}^{(2)}}{n \sin(n\alpha)}, \quad (8.3a)$$

$$G_n = -\frac{A_{n-1}^{(1)}}{n}, \quad (8.3b)$$

for $n \geq 1$. While λ_0 remains arbitrary, it can be fixed by an additional boundary condition, such as the value of $c(\rho = 0)$. Then we get $c(\rho = 0) = \lambda_0$. The condition for existence of F_n and G_n such that boundary conditions can be satisfied by this ansatz is $\sin(n\alpha) \neq 0$ (i.e. $\alpha \neq q\pi$, where $q \in \mathbb{Q}^+$). If $\sin(n\alpha) = 0$, then a more general ansatz is required. Alternatively, we note that the above ansatz is sufficient if $\alpha = r\pi$ for $r \in \mathbb{R}^+ \setminus \mathbb{Q}^+$. Then r

can be taken to be e.g. $r = q \pm \sqrt{2} \times 10^{-n}$, where n can be arbitrarily large, and we obtain a solution for the desired angle $\alpha = q\pi$ in the limit of large n .

9. Discussion and conclusions

In this paper, inspired by Moffatt eddies (Moffatt 1964a,b) that emerge in wedge-like geometries under mechanical boundary forcing, we have shown that corner geometry with chemically active sectors can be used to generate similar eddies. Our solution involved the exact solution of the diffusion problem in the wedge geometry using the Mellin transform formalism, followed by a solution of the biharmonic equation for the stream function of the associated flow. The proposed diffusio-osmotic framework relies on a fixed-flux boundary condition for the solute release from a catalytic patch, which is appropriate when the diffusion of the solute is much faster than its adsorption (i.e. in the limit of low Damköhler number) and the advection is slow compared to diffusion (corresponding to the limit of low Péclet number).

In the simple case of uniform coverage of the walls with chemical activity, the geometric asymmetry alone is responsible for heterogeneous distribution of solute concentration, which drives the flow. In such a setting, the problem admits a simple analytical solution akin to the classical Taylor's scraper problem when one wall is chemically active. Similarly, an analytical solution is also available when both walls are covered with catalyst. These solutions can serve as benchmarks for numerical computations, particularly when solving for the concentration field with non-trivial active boundary conditions.

In the more general case, where patches of activity are distributed on the walls, we presented a solution technique using the Mellin transform to solve the diffusion problem, and subsequently find the coefficients of the general solution of the associated flow problem. The solutions can be evaluated numerically for an arbitrary distribution of patches and a combination of boundary conditions.

We note here that while our present work bears resemblance to the previously analysed case of flow in a two-dimensional confined channel of Visan *et al.* (2024) in the limit $\alpha \rightarrow \pi$ with a single active sector, a straightforward comparison is not possible. In our case, there is a single wall, and the concentration field decays monotonically with the distance from the active patch, while Visan *et al.* (2024) consider a system confined between two walls; the bottom surface is patterned with activity, and they impose a Dirichlet boundary condition of constant concentration on the top wall. Additionally, they assume periodic boundary conditions in the direction parallel to the walls. They then observe a pair of counter-rotating vortices. In our system, with only one surface being present for $\alpha = \pi$, we see similar flow structure in the vicinity of an active patch. However, the presence of the top boundary in their system introduces an additional length scale (apart from the size of the active patch itself) that sets the size of recirculating vortices. This interplay of length scales is further discussed by Michelin & Lauga (2019). In the absence of the top confining wall, we see different asymptotics of the concentration field (decay with the distance), and the recirculation zone becomes larger but the flow strength decays faster away from the patch.

To assess the practical relevance of our theoretical results, we estimate the expected flow velocities in a potential experimental realisation of our model. The typical slip velocity, defined in (2.2), is given by the product of the surface mobility \mathcal{M} and the normal gradient of solute concentration. Following the classical 1947 analysis of Derjaguin *et al.* (reprinted in Derjaguin *et al.* 1993), the magnitude of the surface slip velocity can be approximated as $u \sim (k_B T / \eta) K L^* \nabla_{\parallel} c$, where $\nabla_{\parallel} c$ is the tangential concentration gradient along the active surface, $k_B T$ is the thermal energy, η is the viscosity, and K and L^* are

parameters characterising the solute distribution profile in the boundary layer adjacent to the surface. For uncharged solute molecules, this profile arises from surface interactions such as van der Waals and dipole forces, as well as excluded volume effects. Using the representative value $KL^* \approx 6 \times 10^{-16} \text{ cm}^2$ reported by Anderson (1989), together with a realistic concentration gradient 0.1 mol cm^{-4} in water at room temperature, we obtain slip velocities approximately $u_s \sim 2 \mu\text{m s}^{-1}$. This estimate is comparable to typical flow speeds in microchannels. As illustrated in figures 7 and 8, the azimuthal velocity component reaches a substantial fraction of this value, indicating that boundary actuation represents a feasible mechanism for flow control.

We note that our solution can also be applied as an approximation in finite geometries, such as that of a rectangular microfluidic channel with chemically patterned corners. When active sectors are contained in the region of a corner (with $\alpha = \pi/2$) such that $\rho < b_{max}$, the concentration field away from the active region asymptotically behaves as $c(\rho, \theta) \sim (b_{max}/\rho)^2$. Thus the slip velocity due to chemically active sectors scales as $|u_s| \sim (b_{max}/\rho)^3$. Note that for such approximation to apply to finite domains, total solute flux away from the chemically active region has to vanish. It can be verified that (6.18) is a sufficient condition for the total flux to vanish for $\rho > b_{max}$, and the local solute current asymptotically scales as $(b_{max}/\rho)^3$. In the limit of well-separated chemically active corners, one can superpose the solutions from neighbouring corners, and as a result produce the streamline pattern for a more complex channel shape.

Our findings thus may have direct implications for microfluidic applications, particularly in small-scale mixing and catalytic processes. Recent studies by Munteanu *et al.* (2020) and Popescu *et al.* (2025) demonstrated that patches of glucose oxidase (GOX) imprinted on planar surfaces can generate surface slip flows through enzymatic decomposition of glucose solutions. The resulting chemical gradients produce diffusio-osmotic slip velocities of the order of $1-10 \mu\text{m s}^{-1}$, providing a realistic example of active surfaces suitable for the geometries considered here. Moreover, it has been shown that inhomogeneous distribution of solute in dead-end pores can enhance the diffusio-phoretic removal of colloids from confined spaces (Li, Alipour & Pahlavan 2025), and the proposed corner design offers a way to achieve this heterogeneity without moving parts. Although the present framework is developed for osmotic flows, the underlying mechanism is general and may be extended to other phoretic/osmotic effects such as electrophoresis or thermophoresis. These mechanisms can similarly generate surface gradients that drive macroscopic flow in wedge-shaped cavities or microfluidic channels with slanted walls. Given that diffusio-osmosis has already been proposed as a mechanism for nanoscale pumping (Chanda & Tsai 2022) and for guiding the migration of biomolecules, blood cells and vesicles into microcavities (Vrhovec Hartman *et al.* 2018), we offer here a new geometric configuration for directed transport. When combined with external control methods – such as intensity-tuned photocatalysis (Timmerhuis 2022), enzymatic activity (Popescu *et al.* 2025) or light-activated diffusio-osmosis (Muraveva *et al.* 2024) – the proposed geometry offers a promising platform for the coupled hydrodynamic and chemical manipulation of particles in confined corner flows.

Funding. This research was supported by the National Science Centre of Poland Sonata Bis grant no. 2023/50/E/ST3/00465 to M.L.

Declaration of interests. The authors report no conflict of interest.

Data availability statement. The Mathematica notebooks used to compute the results of this study are openly available in Zenodo at <https://doi.org/10.5281/zenodo.17800756>.

REFERENCES

ABÉCASSIS, B., COTTIN-BIZONNE, C., YBERT, C., AJDARI, A. & BOCQUET, L. 2008 Boosting migration of large particles by solute contrasts. *Nat. Mater.* **7** (10), 785–789.

AKDENIZ, B., WOOD, J.A. & LAMMERTINK, R.G.H. 2023 Diffusiophoresis and diffusio-osmosis into a dead-end channel: role of the concentration-dependence of zeta potential. *Langmuir* **39** (6), 2322–2332.

ALESSIO, B.M., SHIM, S., MINTAH, E., GUPTA, A. & STONE, H.A. 2021 Diffusiophoresis and diffusioosmosis in tandem: two-dimensional particle motion in the presence of multiple electrolytes. *Phys. Rev. Fluids* **6** (5), 054201.

ALIPOUR, M., LI, Y., LIU, H. & PAHLAVAN, A.A. 2024 Diffusiophoretic transport of colloids in porous media. [arXiv:2411.14712](https://arxiv.org/abs/2411.14712).

ANDERSON, J.L. 1989 Colloid transport by interfacial forces. *Annu. Rev. Fluid Mech.* **21**, 61–99.

ANTUNES, G.C., M ALGARETTI, P. & HARTING, J. 2023 Turning catalytically active pores into active pumps. *J. Chem. Phys.* **159** (13), 134903.

ANTUNES, G.C., M ALGARETTI, P., HARTING, J. & DIETRICH, S. 2022 Pumping and mixing in active pores. *Phys. Rev. Lett.* **129** (18), 188003.

ARCHER, R.J., CAMPBELL, A.I. & EBBENS, S.J. 2015 Glancing angle metal evaporation synthesis of catalytic swimming Janus colloids with well defined angular velocity. *Soft Matt.* **11** (34), 6872–6880.

ARFKEN, G.B., WEBER, H.J. & HARRIS, F.E. 2013 Chapter 10 - Green's functions. In *Mathematical Methods for Physicists (Seventh Edition)*, 7th edn, pp. 447–467. Academic Press.

AULT, J.T., SHIN, S. & STONE, H.A. 2018 Diffusiophoresis in narrow channel flows. *J. Fluid Mech.* **854**, 420–448.

BATCHELOR, G.K. 2000 *An Introduction to Fluid Dynamics*. Cambridge University Press.

BATTAT, S., AULT, J.T., SHIN, S., KHODAPARAST, S. & STONE, H.A. 2019 Particle entrainment in dead-end pores by diffusiophoresis. *Soft Matt.* **15** (19), 3879–3885.

BECHINGER, C., DI LEONARDO, R., LÖWEN, H., REICHHARDT, C., VOLPE, G. & VOLPE, G. 2016 Active particles in complex and crowded environments. *Rev. Mod. Phys.* **88** (4), 045006.

BHATTACHARYYA, S., SENGUPTA, S. & CHAKRABORTY, S. 2023 Autonomous chemical micropumps driven by self-generated solute gradients. *Langmuir* **39** (5), 1673–1685.

BISWAS, S. & KALITA, J.C. 2018 Moffatt eddies in the driven cavity: a quantification study by an HOC approach. *Comput. Maths Applics.* **76** (3), 471–487.

BUTZER, P.L. & JANSCHE, S. 1997 A direct approach to the Mellin transform. *J. Fourier Anal. Applcs.* **3** (4), 325–376.

CHANDA, S. & TSAI, P.A. 2022 Numerical investigation of diffusioosmotic flow in a tapered nanochannel. *Membranes* **12** (5), 481.

CHU, H.C.W., GAROFF, S., TILTON, R.D. & KHAIR, A.S. 2020 Advective-diffusive spreading of diffusiophoretic colloids under transient solute gradients. *Soft Matt.* **16** (1), 238–246.

CHU, H.C.W., GAROFF, S., TILTON, R.D. & KHAIR, A.S. 2021 Macrotransport theory for diffusiophoretic colloids and chemotactic microorganisms. *J. Fluid Mech.* **917**, A52.

CHU, H.C.W., GAROFF, S., TILTON, R.D. & KHAIR, A.S. 2022 Tuning chemotactic and diffusiophoretic spreading via hydrodynamic flows. *Soft Matt.* **18** (9), 1896–1910.

DADDI-MOUSSA-IDER, A., FISCHER, L., PRADAS, M. & MENZEL, A.M. 2025 Elastic displacements and viscous hydrodynamic flows in wedge-shaped geometries with a straight edge: Green's functions for parallel forces. *Proc. R. Soc. A: Math. Phys. Engng Sci.* **481**, 2322.

DADDI-MOUSSA-IDER, A. & MENZEL, A.M. 2025 Elastic displacements and viscous flows in wedge-shaped geometries with a straight edge: Green's functions for perpendicular forces. *J. Elasticity* **157** (3), 54.

DAUPARAS, J. & LAUGA, E. 2018 Leading-order Stokes flows near a corner. *IMA J. Appl. Maths* **83** (4), 590–633.

DEBNATH, L. & BHATTA, D. 2016 *Integral Transforms and Their Applications*. Chapman and Hall/CRC.

DERJAGUIN, B.V., SIDORENKO, G., ZUBASHCHENKO, E. & KISELEVA, E. 1993 Kinetic phenomena in the boundary layers of liquids 1. The capillary osmosis. *Prog. Surf. Sci.* **43** (1–4), 138–152.

DEVILLE, M.O. 2022 *An Introduction to the Mechanics of Incompressible Fluids*. Springer International Publishing.

DOAN, V.S., CHUN, S.G., FENG, J. & SHIN, S. 2021 Confinement-dependent diffusiophoretic transport of nanoparticles in collagen hydrogels. *Nano Lett.* **21** (18), 7625–7630.

GILPIN, W., BULL, M.S. & PRAKASH, M. 2020 The multiscale physics of cilia and flagella. *Nat. Rev. Phys.* **2** (2), 74–88.

GOLESTANIAN, R., LIVERPOOL, T.B. & AJDARI, A. 2007 Designing phoretic micro- and nano-swimmers. *New J. Phys.* **9**, 126.

HE, X., SUN, Z. & ZHANG, M. 2022 Moffatt eddies in electrohydrodynamics flows: numerical simulations and analyses. *J. Fluid Mech.* **953**, A14.

JOTKAR, M., DE ANNA, P., DENTZ, M. & CUETO-FELGUEROZO, L. 2024 The impact of diffusiophoresis on hydrodynamic dispersion and filtration in porous media. *J. Fluid Mech.* **991**, A8.

JÜLICHER, F. & PROST, J. 2009 Generic theory of colloidal transport. *Eur. Phys. J. E* **29**, 27–36.

KAR, A., CHIANG, T.-Y., ORTIZ RIVERA, I., SEN, A. & VELEGOL, D. 2015 Enhanced transport into and out of dead-end pores. *ACS Nano* **9** (1), 746–753.

KREIENBRINK, K.M., CRUSE, Z.A., KUMARI, A. & SHIELDS, C.W. 2025 Precise surface patches on active particles of arbitrary shape through microstenciling. *Nat. Commun.* **16** (1), 6062.

LI, Y., ALIPOUR, M. & PAHLAVAN, A. 2025 Solute dispersion boosts the phoretic removal of colloids from dead-end pores. arXiv:2510.24938.

LISICKI, M., MICHELIN, S. & LAUGA, E. 2016 Phoretic flow induced by asymmetric confinement. *J. Fluid Mech.* **799**, R5.

LISICKI, M., REIGH, S.Y. & LAUGA, E. 2018 Autophoretic motion in three dimensions. *Soft Matt.* **14** (17), 3304–3314.

LIU, C.H. & JOSEPH, D.D. 1977 Stokes flow in wedge-shaped trenches. *J. Fluid Mech.* **80**, 443.

MARTIN, P.A. 2017 On mixed boundary-value problems in a wedge. *Q. J. Mech. Appl. Maths* **70** (4), 373–386.

MEYER, C.R. & CREYTS, T.T. 2017 Formation of ice eddies in subglacial mountain valleys. *J. Geophys. Res.: Earth Surf.* **122** (9), 1574–1588.

MICHELIN, S. & LAUGA, E. 2014 Phoretic self-propulsion at finite Péclet numbers. *J. Fluid Mech.* **747**, 572–604.

MICHELIN, S. & LAUGA, E. 2015 Autophoretic locomotion from geometric asymmetry. *Eur. Phys. J. E* **38**, 7.

MICHELIN, S. & LAUGA, E. 2019 Universal optimal geometry of minimal phoretic pumps. *Sci. Rep. UK* **9** (1), 10788.

MICHELIN, S., MONTENEGRO-JOHNSON, T.D., DE CANIO, G., LOBATO-DAUZIER, N. & LAUGA, E. 2015 Geometric pumping in autophoretic channels. *Soft Matt.* **11**, 5804–5811.

MICHELL, J.H. 1899 On the direct determination of stress in an elastic solid, with application to the theory of plates. *Proc. Lond. Math. Soc.* **s1-31** (1), 100–124.

MIGACZ, R.E., CASTLEBERRY, M. & AULT, J.T. 2024 Enhanced diffusiophoresis in dead-end pores with time-dependent boundary solute concentration. *Phys. Rev. Fluids* **9** (4), 044203.

MOFFATT, H.K. 1964a Viscous and resistive eddies near a sharp corner. *J. Fluid Mech.* **18** (1), 1–18.

MOFFATT, H.K. 1964b Viscous eddies near a sharp corner. *Arch. Mech. Stosowanej* **2** (16), 365–372.

MUNTEANU, R.-E., POPESCU, M.N. & GÁSPÁR, S. 2020 The impact of geometrical confinement in a slab on the behavior of tracer particles near active glucose oxidase micropump. *Colloid Polym. Sci.* **299** (2), 297–306.

MURAVEVA, V., LOMADZE, N., GORDIEVSKAYA, Y.D., ORTNER, P., BETA, C. & SANTER, S. 2024 Manipulation of artificial and living small objects by light driven diffusioosmotic flow. *Sci. Rep. UK* **14** (1), 18342.

OMORI, T. & ISHIKAWA, T. 2025 Ciliary fluid dynamics of swimming, feeding, pumping, and sensing. *Phys. Rev. Fluids* **10** (8), 080501.

PALACCI, J., ABÉCASSIS, B., COTTIN-BIZONNE, C., YBERT, C. & BOCQUET, L. 2010 Colloidal motility and pattern formation under rectified diffusiophoresis. *Phys. Rev. Lett.* **104** (13), 138302.

POLYCHRONOPOULOS, N.D. & VLACHOPOULOS, J. 2018 Computer flow simulation of Moffatt eddies in single screw extrusion. *Intl Polym. Process.* **33** (5), 662–668.

POPESCU, M.N., NICOLA, B.A., USPAL, W.E., DOMÍNGUEZ, A. & GÁSPÁR, S. 2025 Hydrodynamic Stokes flow induced by a chemically active patch imprinted on a planar wall. *J. Colloid Interface Sci.* **690**, 137296.

RAYNAL, F., BOURGOIN, M., COTTIN-BIZONNE, C., YBERT, C. & VOLK, R. 2018 Advection and diffusion in a chemically induced compressible flow. *J. Fluid Mech.* **847**, 228–243.

RAYNAL, F. & VOLK, R. 2019 Diffusiophoresis, Batchelor scale and effective Péclet numbers. *J. Fluid Mech.* **876**, 818–829.

SABASS, B. & SEIFERT, U. 2012 Dynamics and efficiency of a self-propelled, diffusiophoretic swimmer. *J. Chem. Phys.* **136**, 064508.

SAMBAMOORTHY, S. & CHU, H.C.W. 2023 Diffusiophoresis of a spherical particle in porous media. *Soft Matt.* **19** (6), 1131–1143.

SAMBAMOORTHY, S. & CHU, H.C.W. 2025 Diffusiophoresis in porous media saturated with a mixture of electrolytes. *Nanoscale Adv.* **7** (7), 2057–2067.

SENGUPTA, S., PATRA, D., ORTIZ-RIVERA, I., AGRAWAL, A., SHKLYAEV, S., DEY, K.K., CÓRDOVA-FIGUEROA, U., MALLOUK, T.E. & SEN, A. 2014 Self-powered enzyme micropumps. *Nat. Chem.* **6** (5), 415–422.

SHANKAR, P.N. 2005 Moffatt eddies in the cone. *J. Fluid Mech.* **539**, 113–135.

SHI, N., NERY-AZEVEDO, R., ABDEL-FATTAH, A.I. & SQUIRES, T.M. 2016 Diffusiophoretic focusing of suspended colloids. *Phys. Rev. Lett.* **117** (25), 258001.

SHIM, S. 2022 Diffusiophoresis, diffusioosmosis, and microfluidics: surface-flow-driven phenomena in the presence of flow. *Chem. Rev.* **122** (7), 6986–7009.

SHIN, S., UM, E., SABASS, B., AULT, J.T., RAHIMI, M., WARREN, P.B. & STONE, H.A. 2016 Size-dependent control of colloid transport via solute gradients in dead-end channels. *Proc. Natl Acad. Sci. USA* **113** (2), 257–261.

SOMASUNDAR, A., QIN, B., SHIM, S., BASSLER, B.L. & STONE, H.A. 2023 Diffusiophoretic particle penetration into bacterial biofilms. *ACS Appl. Mater. Interfaces* **15** (28), 33263–33272.

SPRENGER, A.R. & MENZEL, A.M. 2023 Microswimming under a wedge-shaped confinement. *Phys. Fluids* **35** (12), 123119.

SQUIRES, T.M. & QUAKE, S.R. 2005 Microfluidics: fluid physics at the nanoliter scale. *Rev. Mod. Phys.* **77**, 977.

STAFFELD, P.O. & QUINN, J.A. 1989 Diffusion-induced banding of colloid particles via diffusiophoresis. *J. Colloid Interface Sci.* **130** (1), 69–87.

STROOCK, A.D., WECK, M., CHIU, D.T., HUCK, W.T.S., KENIS, P.J.A., ISMAGILOV, R.F. & WHITESIDES, G.M. 2000 Patterning electro-osmotic flow with patterned surface charge. *Phys. Rev. Lett.* **84** (15), 3314–3317.

STROOCK, A.D. & WHITESIDES, G.M. 2003 Controlling flows in microchannels with patterned surface charge and topography. *Accounts Chem. Res.* **36**, 597–604.

TANEDA, S. 1979 Visualization of separating Stokes flows. *J. Phys. Soc. Japan* **46** (6), 1935–1942.

TAYLOR, G.I. 1962 On scraping viscous fluid from a plane surface. In *Miszellaneen der angewandten Mechanik: Festschrift Walter Tollmien zum 60. Geburtstag am 13. Oktober 1960 von seinen Freunden und Schülern* (ed. M. Schäfer), pp. 313–315. De Gruyter.

TENG, J., RALLABANDI, B. & AULT, J.T. 2023 Diffusioosmotic dispersion of solute in a long narrow channel. *J. Fluid Mech.* **977**, A5.

TIMMERHUIS, N. 2022 Turn on the light: diffusio-osmosis induced by photocatalytic reactions. PhD thesis, University of Twente, Enschede, Netherlands.

TIWARI, K., DHAKAR, J., UPADHYAYA, K. & CHOUDHARY, A. 2025 Influence of electrolytic gradient orientation on phoretic transport in dead-end pores. *Langmuir* **41** (28), 18583–18596.

TRANTER, C.J. 1948 The use of the Mellin transform in finding the stress distribution in an infinite wedge. *Q. J. Mech. Appl. Maths* **1** (1), 125–130.

VISAN, A., WOOD, J.A. & LAMMERTINK, R.G.H. 2024 Enhancing conversion using diffusio-osmosis from patterned catalytic surfaces. *Ind. Chem. Mater.* **2** (3), 451–457.

VOLK, R., BOURGOIN, M., BRÉHIER, C.-É. & RAYNAL, F. 2022 Phoresis in cellular flows: from enhanced dispersion to blockage. *J. Fluid Mech.* **948**, A42.

VRHOVEC HARTMAN, S., BOŽIĆ, B. & DERGANC, J. 2018 Migration of blood cells and phospholipid vesicles induced by concentration gradients in microcavities. *New Biotechnol.* **47**, 60–66.

WILSON, J.L., SHIM, S., YU, Y.E., GUPTA, A. & STONE, H.A. 2020 Diffusiophoresis in multivalent electrolytes. *Langmuir* **36** (25), 7014–7020.

YU, T., ATHANASSIADIS, A.G., POPESCU, M.N., CHIKKADI, V., GÜTH, A., SINGH, D.P., QIU, T. & FISCHER, P. 2020 Microchannels with self-pumping walls. *ACS Nano* **14** (10), 13673–13680.